crystals

MDPI

Article

Crystal Structural Analysis of DL-Mandelate Salt of Carvedilol and Its Correlation with Physicochemical Properties

Nanami Hata, Takayuki Furuishi, Majid I. Tamboli, Momiji Ishizaki, Daiki Umeda, Kaori Fukuzawa and Etsuo Yonemochi *

Department of Physical Chemistry, School of Pharmacy and Pharmaceutical Sciences, Hoshi University, 2-4-41 Ebara, Shinagawa-ku, Tokyo 142-8501, Japan; m1712@hoshi.ac.jp (N.H.); t-furuishi@hoshi.ac.jp (T.F.); t-majid@hoshi.ac.jp (M.I.T.); s141015@hoshi.ac.jp (M.I.); m1802@hoshi.ac.jp (D.U.); k-fukuzawa@hoshi.ac.jp (K.F.)

* Correspondence: e-yonemochi@hoshi.ac.jp; Tel.: +81-3-5498-5048

Received: 21 December 2019; Accepted: 16 January 2020; Published: 20 January 2020

Abstract: A 1:1 salt of carvedilol (CVD), an anti-hypertensive drug, with DL-mandelic acid (DL-MA) was crystallized from ethanol and the structure was characterized by X-ray single-crystal diffraction, revealing salt formation by transfer of an acidic proton from the COOH group of MA to the aliphatic (acyclic) secondary amino NH group of CVD. The crystal structure is triclinic, with a P-1 space group and unit cell parameters a = 9.8416(5) Å, b = 11.4689(5) Å, c = 14.0746(7) Å, α = 108.595(8), β = 95.182(7), γ = 107.323(8), V = 1406.95(15) Å^3, and Z = 2. The asymmetric unit contained one protonated CVD and one MA anion, linked via an N^+–H···O^- strong hydrogen bond and a ratio of 1:1. As previously reported, the thermal, spectroscopic, and powder X-ray diffraction properties of the salt of CVD with DL-MA (CVD_DL-MA) differed from CVD alone. The intrinsic dissolution rate of CVD_DL-MA was about 10.7 times faster than CVD alone in a pH 6.8 buffer.

Keywords: carvedilol; DL-mandelic acid; salt; crystal structure; solubility

1. Introduction

In recent years, the use of crystal engineering to prepare multi-component crystals of pharmaceutically important drug molecules [1–8], agrochemicals [9], pigments [10,11], and explosive materials [12–14] has been widely investigated owing to potential applications in the modification of the physicochemical properties, such as solubility, stability, and bioavailability. Among them, pharmaceutical drug molecules are extremely significant as more than 40% of marketed drug molecules suffer solubility issues [15–17]. Constant and continuous efforts directed toward the development of various techniques to improve solubility of the active pharmaceutical ingredient (API) include particle size reduction [18–20], solid dispersion with excipient [21,22], complexation with cyclodextrin [23], polymorph screening, as well as the preparation of multi-component crystals, with generally safe coformers approved by the FDA. In recent years, related research has been widely spread in literature [24–29]. Multi-component crystals of API enhance physicochemical properties such as solubility, bioavailability, and stability, and are becoming very popular due to how they neither replace nor modify the parent API component. Carvedilol (CVD), (±)-1-(carbazol-4-yloxy)-3-[[2-(omethoxyphenoxy) ethyl] amino]-2-propanol, is widely using in the treatment of hypertension, or mild to severe heart failure [30–32]. CVD belongs to the Biopharmaceutics Classification System (BCS) class II and has low solubility and high permeability [33]. CVD is a remarkable potential drug to improve solubility and bioavailability, with several approaches

attempted in the present literature [34–40]. Furthermore, CVD is known to exhibit polymorphism, with three polymorphic forms reported in the literature [41]. Salt and cocrystal preparation remain potential methods to improve solubility; however, salt formation is considered to be superior for improving aqueous solubility [42,43]. Syntheses of various pharmaceutical salts of CVD, with pharmaceutically acceptable organic acids and physicochemical properties, have been reported in literature, indicating a 1.78-fold increase in the solubility of fumaric acid salt [40]. Interestingly, reports have indicated that the solvent depended two polymorphic forms of the mandelate salt with CVD, demonstrating a monotropic relation between them based on thermal analysis and a slurry experiment [40]. Furthermore, these polymorphs were characterized by powder X-ray diffraction (PXRD), differential scanning calorimetry (DSC), thermogravimetric (TG) analysis, Fourier-transform infrared spectroscopy (FT-IR), and scanning electron microscopy [40]. However, no report has investigated the X-ray single-crystal structure of either of the polymorphic forms of this salt. Our ongoing research is focused on improving the physicochemical properties of pharmaceutical drug molecules by inducing multi-component crystals, such as cocrystals, salt, and its solvates [44–48]. Moreover, we aim to establish new crystalline solid forms of the API. In this report, we discuss our efforts to improve the solubility of CVD by preparing its crystalline salts with DL-mandelic acid (DL-MA) (Figure 1), and we evaluate the X-ray single-crystal structure of stable Form I of the DL-mandelate salt of CVD (CVD_DL-MA), crystal structural analysis, and its physiochemical characteristics.

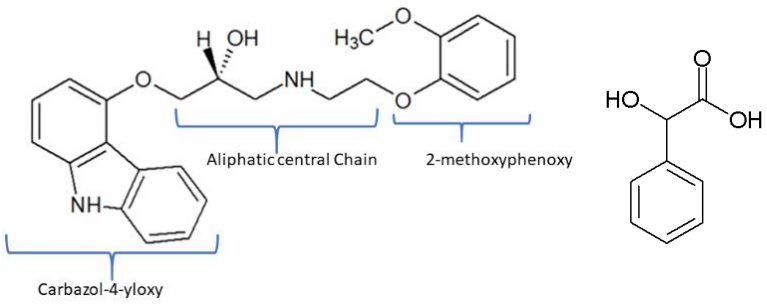

(**a**) (**b**)

Figure 1. Structures of racemic carvedilol (CVD) ((**a**), one enantiomer shown for clarity)) and DL-mandelic acid (DL-MA) (**b**).

2. Materials and Methods

2.1. Materials

CVD (Form II) and DL-MA were purchased from Tokyo Chemical Industry Co. Ltd. (Tokyo, Japan). All other analytical-grade solvents and reagents were commercially obtained and used without further purification.

2.2. Preparation of CVD Salts

The physical mixture of CVD and DL-MA (molar ratio = 1:1) was dissolved in ethanol and the ethanol was completely removed using a rotary evaporator. Next, the residual substance was dissolved in ethanol, and the resulting solution was maintained at ambient temperature for one week, yielding a colorless block-shaped crystal.

2.3. Single-Crystal X-Ray Diffraction

The single-crystal X-ray diffraction data were collected at 123 K for CVD_DL-MA. The measurements were carried out in ω-scan mode with an R-AXIS RAPID II (Rigaku, Tokyo, Japan) using the Cu-Kα X-ray obtained from rotating the anode source with a graphite monochromator. The integrated and scaled data were empirically corrected for absorption effects using ABSCOR [49].

The initial structure was solved using the direct method with SIR 2004 and refined on Fo^2 with SHELXL 2014 [50,51]. All non-hydrogen atoms were refined anisotropically. The hydrogen atom attached to the oxygen O5, and the nitrogen N1 atom, were located using the differential Fourier map. All other hydrogen atom positions were calculated geometrically and included in the calculation using the riding atom model. All the hydrogen atoms were refined isotropically. The molecular graphics were produced using Mercury 3.7 software [52]. CCDC 1972926 contains the supplementary crystallographic data for the CVD_DL-MA, and can be obtained free of charge from the Cambridge Crystallographic Data Centre via https://www.ccdc.cam.ac.uk/structures/.

2.4. Powder X-Ray Diffraction (PXRD)

PXRD patterns were collected using a Rigaku SmartLab diffractometer (Rigaku, Tokyo, Japan) equipped with a Cu-Kα source, parallel beam optics, and a one-dimensional semiconductor array detector (Rigaku D/tex ultra, Rigaku, Tokyo, Japan). The corresponding PXRD patterns were collected in reflection mode for 2θ = 5–40° at 25 °C, with a step of 0.01° and a scan speed of 20° min^{-1} (Cu-Kα source, 45 kV, 200 mA).

2.5. Differential Scanning Calorimetry (DSC) and Thermogravimetric (TG) Measurements

DSC and TG measurements were carried out with Thermo plus EVO2-DSC 8230 and Thermo plus EVO2-TG8120 TG-DTA, respectively (Rigaku Co., Tokyo, Japan). The DSC sample (3 mg) was placed in an aluminum crimped pan, and the TG sample (10 mg) was placed into an aluminum open pan, and they were measured at a speed of 5 °C/min from 25 to 250 °C under nitrogen gas (flow rate = 50 mL/min). Al_2O_3 was used as a reference.

2.6. Fourier-Transform Infrared Spectroscopy (FT-IR)

The infrared spectra of samples were obtained using FT-IR (FT-IR-4200 spectrometer, JASCO Co., Tokyo, Japan) with an attenuated total reflection (ATR) unit (ATR-PRO670H-S, JASCO Co.). The spectrum recorded represents an average of 64 scans obtained with a resolution of 4 cm^{-1} at room temperature. The spectra were collected in the wavenumber range from 4000–400 cm^{-1}. The internal reflectance element used in this study was a diamond trapezoid with 45° entrance and exit faces.

2.7. Solubility Tests

2.7.1. Equilibrium Solubility Experiments

Equilibrium solubility experiments were carried out using the flask shaking method. Before the solubility test, all samples were sieved using standard mesh sieves (mesh size 150 μm) to provide powders with similar particle size distribution. Each 100 mg of CVD, DL-MA, and CVD_DL-MA (about 100 mg) mixture were added to 3 mL phosphate buffer, pH 6.8 (JP 17), and mechanically shaken (120 times/min, Personal Lt-10f, Taitec corporation, Saitama, Japan) for 24 h at 37 °C. The supernatant was filtered (pore size: 0.45 μm) and the CVD concertation was determined by HPLC. The results are expressed as the mean ± standard deviation (SD) of at least three independent experiments.

2.7.2. Intrinsic Dissolution Experiment

The dissolution studies were carried out using the paddle method with a dissolution tester (NTR-3000, TOYAMA SANGYO CO., LTD., Osaka, Japan), and the paddle rotating speed was 100 rpm. Prior to the dissolution test, CVD and CVD_DL-MA were sieved using standard mesh sieves (mesh size 150 μm) and then the excess from the samples was added to a vessel filled with 500 mL PBS (pH 6.8) at 37 °C. Samples (9 mL) were withdrawn and filtered (0.45 μm) for analysis at specified time points, and assessed for CVD content by the HPLC method. Results are expressed as the mean ± standard deviation (SD) of at least three independent experiments.

2.8. High-Performance Liquid Chromatography (HPLC) Conditions

The HPLC comprises a PU-plus intelligent HPLC pump, a UV-intelligent UV/VIS detector, a CO-2060 plus intelligent column oven, an AS-2055 plus intelligent sampler, and a ChromNAV chromatography data system Ver. 1.08 (all from JASCO, Tokyo, Japan). The analytical column, a J-Pak Vario XBP C8-T (250 × 4.6 mm i.d., particle size 5 µm, from JASCO) was used at 55 °C. The mobile phase consisted of 0.05 M of phosphate buffer (pH 5.0) and acetonitrile (70:30, v/v) at a flow rate of 1.2 mL/min. The injection volume was 10 µL. The column eluate was monitored using a visible wavelength of 240 nm.

3. Results and Discussion

3.1. Crystal Structure

CVD was presented as a flexible molecule, with the central aliphatic chain attached to one terminal by carbazol-4-yloxy and other by the 2-methoxyphenoxy moiety as seen in Figure 1. As CVD has hydrogen acceptor and donor sites, the probability of forming a multi-component crystal was higher. From the crystal engineering point of view, CVD could be a potential candidate for exploring various conformations in its different crystalline forms, such as polymorph, salt, cocrystal, and solvates. In the present study, the API was CVD, and DL-MA was the coformer. The salt formation was as expected based on the basic rule of three, the ΔpKa difference between the CVD (pka 7.8) and DL-MA (pka 3.41) was more than three, and its experimental validation in the formation and characterization of salt has been reported [40]. However, the single-crystal structure was not determined. The X-ray single-crystal structure determination and the study of non-covalent interaction within is important, as this reflects the physical properties, and the structural information generated encourages further modification in achieving the desired properties. The X-ray single-crystal structure confirmed the formation of salt with approximately similar C–O bond lengths (1.247(2), 1.266(2) Å) of the (COO^-) carboxylate group of DL-MA. These similarities in the bond length of C–O confirmed the transfer of an acidic proton from DL-MA to the aliphatic (acyclic) secondary amino group of CVD. CVD_DL-MA crystalized in the triclinic *P*-1 space group contains one molecule of each in the asymmetric unit and is linked by strong N^+–H···O^- hydrogen bonds, revealing the molecular salt in the 1:1 molar ratio (Figure 2). The crystallographic information and geometrical parameters for the hydrogen bonding interaction are summarized in Tables 1 and 2.

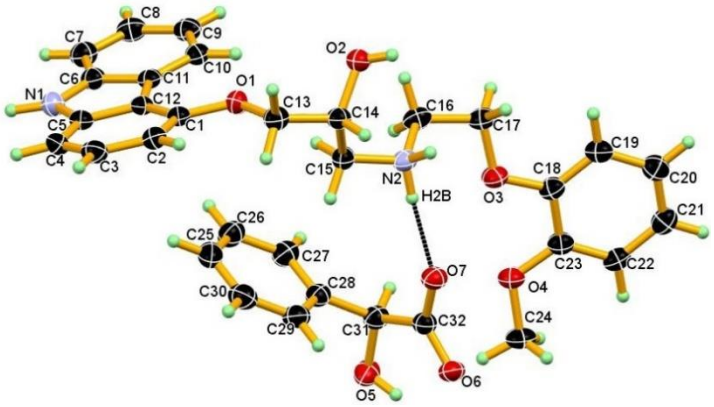

Figure 2. ORTEP diagram of CVD and DL-MA in salt showing the atom numbering scheme. Thermal ellipsoid drawing of CVD and DL-MA in salt drawn at 50% probability level, and H-atoms are shown as small spheres with arbitrary radii.

Table 1. Crystallographic data table for the CVD_DL-MA salt.

Parameters	CVD_DL-MA
Empirical formula	C_{32} H_{34} N_2 O_7
Formula weight	558.61
Temperature	123(2) K
Wavelength	1.54187 Å
Crystal system	Triclinic
Space group	*P* −1
Unit cell dimensions	*a* = 9.8416(5) Å, *α* = 108.595(8)°
	b = 11.4689(5) Å, *β* = 95.182(7)°
	c = 14.0746(7) Å, *γ* = 107.323(8)°
Volume	1406.95(15) $Å^3$
Z	2
Density (calculated)	1.319 Mg/m^3
Absorption coefficient	0.764 mm^{-1}
F(000)	592
Crystal size	0.210 × 0.150 × 0.100 mm^3
Theta range for data collection	3.385° to 68.184°
Index ranges	−11<=h<=11, −13<=k<=13, −16<=l<=16
Reflections collected	16381
Independent reflections	5033 [R(int) = 0.0359]
Completeness to theta = 67.687°	97.9%
Absorption correction	Semi-empirical from equivalents
Max. and min. transmission	0.926 and 0.605
Refinement method	Full-matrix least-squares on F^2
Data / restraints / parameters	5033/0/380
Goodness-of-fit on F^2	1.056
Final R indices [I>2sigma(I)]	R_1 = 0.0468, wR_2 = 0.1252
R indices (all data)	R_1 = 0.0626, wR_2 = 0.1352
Extinction coefficient	n/a
Largest diff. peak and hole	0.356 and −0.227 e.$Å^{-3}$

Table 2. Geometrical parameters of the hydrogen bond interaction in salt CVD_DL-MA.

D-H···A	D-H (Å)	H···A (Å)	D···A (Å)	D-H···A (°)	Symmetry codes
N1-H1AA···O5	0.99(3)	1.87(3)	2.848(2)	169(2)	−x, −y, −z
N2-H2A···O7	0.91	1.80	2.699(2)	168	1 − x,1 − y,1 − z
N2-H2B···O7	0.91	1. 91	2.741(2)	151	*x, y, z*
O2-H2B···O6	0.84	1.89	2.7164(18)	168	1 − x,1 − y,1 − z
C24-H24A···O2	0.98	2.66	3.418(3)	134	*x, 1 + y, z*
O5-5HA···Cg2	0.90(3)	2.74(3)	3.1361(19)	108(2)	*x, 1 + y, z*
C8-H8···O6	0.95	2.65	3.383(2)	134	−1 + x, −1 + y, z
C9-H9···O2	0.95	2.68	3.597	163	−x, −y, 1 − z
C27-H27···Cg4	0.95	2.85	3.763(2)	163	−x, 1 − y, 1 − z
C13-H13A···Cg4	0.99	2.86	3.603(2)	133	1 − x, 1 − y, 1 − z
C15-H15A···Cg8	0.99	2.69	3.403	129	*x, y, z*

Cg2 centroid of the ring (C1-C2-C3-C4-C5-C12) of carbazol-4-yloxy moiety, Cg4 centroid of the ring (C18-C19-C20-C21-C22-C23) of 2-methoxyphenoxy moiety of CVD and Cg8 centroid of the ring (C25-C26-C27-C28-C29-C30) of MA.

3.2. Crystal Structural Analysis and Its Correlation with Physicochemical Properties

Single-crystal XRD showed the CVD_DL-MA salt crystalized in the triclinic P-1 space group containing one molecule of each in the asymmetric unit, suggesting the molecular salt had a 1:1 molar ratio. The proton was transferred from the COOH group of DL-MA to the aliphatic (acyclic) secondary NH group of CVDs. The conformation of protonated CVD in CVD_DL-MA salt is shown in Figure 2. In the crystal structure of salt, two inversion-symmetry related protonated CVD molecules form dimeric units, bridged by D-MA and L-MA's anions, by using the strong N^+–H···O^- hydrogen

bonds in $R^2_4(8)$ ring motif that involve two acceptor and four donor atoms. In this association, the O7 oxygen atom of both D and L-MA's anion is bifurcated and involved in N^+–H···O^- hydrogen bonding, namely N2–H2A···O7, N2–H2B···O7, with two inversion-symmetry related protonated CVD molecules. Similarly, another oxygen O6 atom of both D and L-MA anions was involved in O–H···O^- hydrogen bonding with a hydroxyl group O2–H2B of protonated CVD molecules, namely a O2–H2B···O6 in $R^4_4(18)$ ring motif involving four donors and four acceptors (Figure 3). Further, this dimeric association also supported by weak C–H··· π contact, namely C13-H13A···Cg4 and C15-H15A···Cg8 interactions.

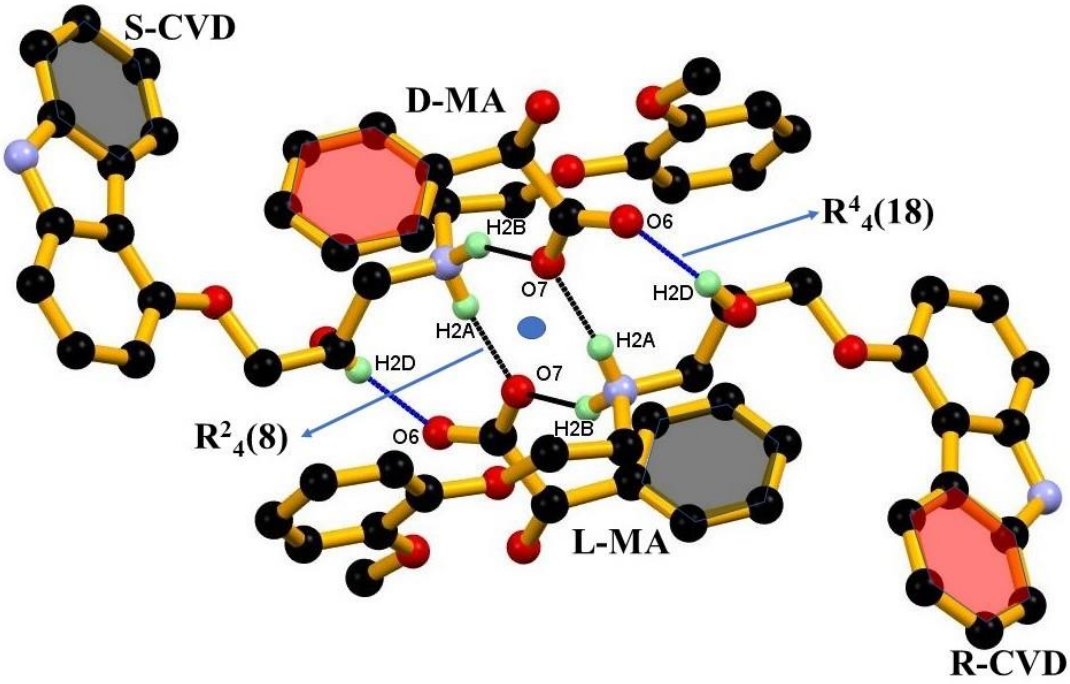

Figure 3. Dimeric units of protonated CVD, bridged by corresponding MA anions in the molecular salt by N2–H2A···O7, N2–H2B···O7 strong hydrogen bonds, which result in the $R^2_4(8)$ ring motif (inner ring), and by O2–H2D···O6, N2–H2B···O7 strong hydrogen bonds, which result in the $R^4_4(18)$ ring motif (outer ring) in the crystal structure of the salt. Blue dot indicates the inversion center and dotted lines indicate the non-covalent interaction (hydrogen atoms not involved in the hydrogen bonding were removed for clarity).

Furthermore, such dimeric units linked via N1–H1AA···O5 hydrogen bonding to the adjacent dimeric units formed a 1D chain, as shown in Figure 4. In this association, the O5 oxygen atom of the mandelate anion formed short and linear hydrogen bonds with N1–H1AA hydrogen atom of the cyclic secondary amino group of carbazol-4-yloxy moiety in protonated CVD.

The neighboring 1D-dimeric chains were assembled into a 2D layer through weak C–H···O and off-centered O–H···π interactions, generating layer packing along the *b*-axis. In this view, H24A methyl hydrogen of protonated CVD formed weak hydrogen bonds, namely C24–H24A···O2, with O2 oxygen of the protonated CVD molecules with similar configuration from the neighboring 1D-dimeric chains along the *b*-axis, and was further supported by weak O–H···π interaction (O5–5HA···Cg2) between hydroxyl group O–H5A of the mandelate anion with the π cloud of aromatic ring (C1-C2-C3-C4-C5-C12) of carbazol-4-yloxy moiety of protonated CVD, as shown in Figure 5.

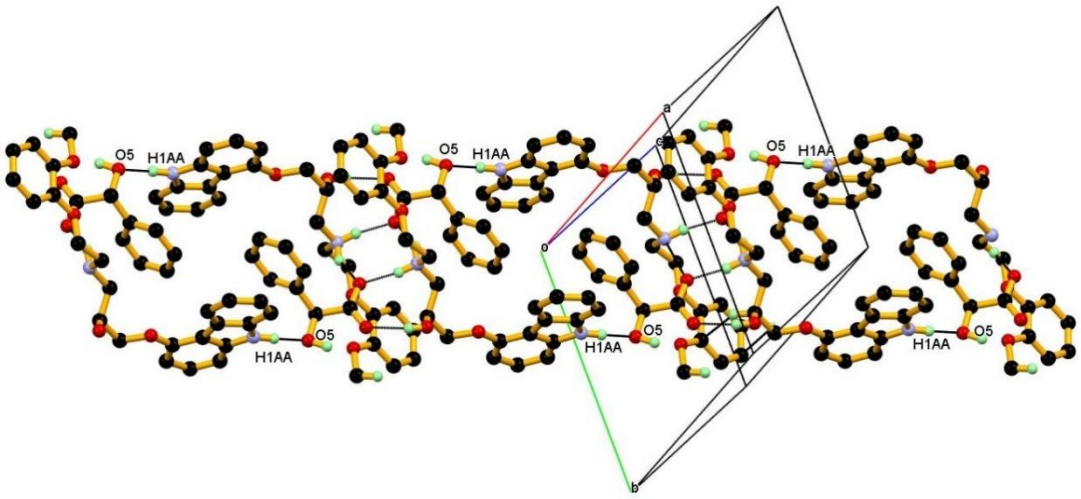

Figure 4. Linking of dimeric units via N1–H1AA···O5 hydrogen bonding to form a 1D-dimeric chain.

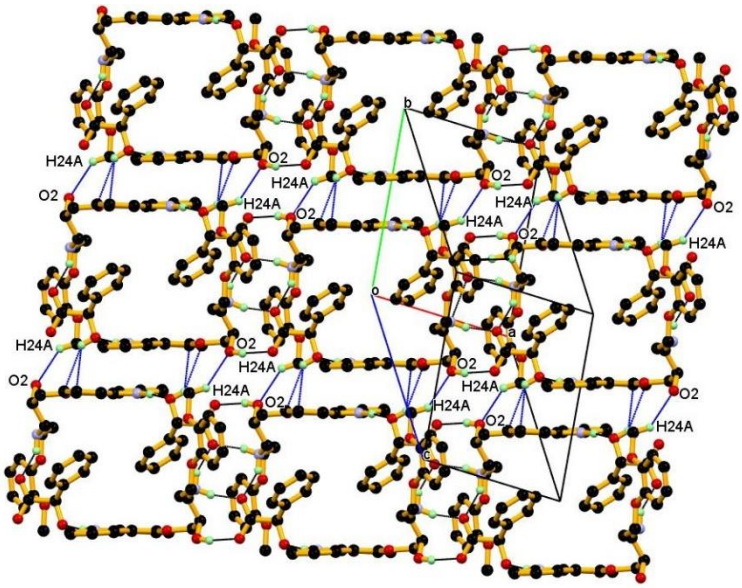

Figure 5. Packing of 1D-dimeric chain via weak C–H···O (C24–H24A···O2) and O–H···π (O5–5HA···Cg2) interaction along *b*-axis. Blue dotted lines indicate an association of neighboring chains.

Neighboring 1D-dimeric chains assembled along the *c*-axis by weak C–H···O hydrogen bonding interaction. In this arrangement, the O2 oxygen atom of protonated CVD formed dimeric hydrogen bonds (C9–H9···O2) with the H9 hydrogen atom of carbazol-4-yloxy moiety of protonated CVD molecules, with the opposite configuration from neighboring chain along the *c*-axis, and further supported by C–H···O^- interaction between the O–6 oxygen atom of the MA anion with the H8 hydrogen atom of carbazol-4-yloxy moiety of protonated CVD (C8–H8···O6), with the resulting packing shown in Figure 6.

Packing of neighboring 1D-dimeric chain along the *a*-axis by weak C–H··· π contact, namely C27–H27···Cg4 interaction between C27–H27 hydrogen of MA anion and π cloud of an aromatic ring (C18-C19-C20-C21-C22-C23) of 2-methoxyphenoxy moiety protonated CVD, shown in Figure 7.

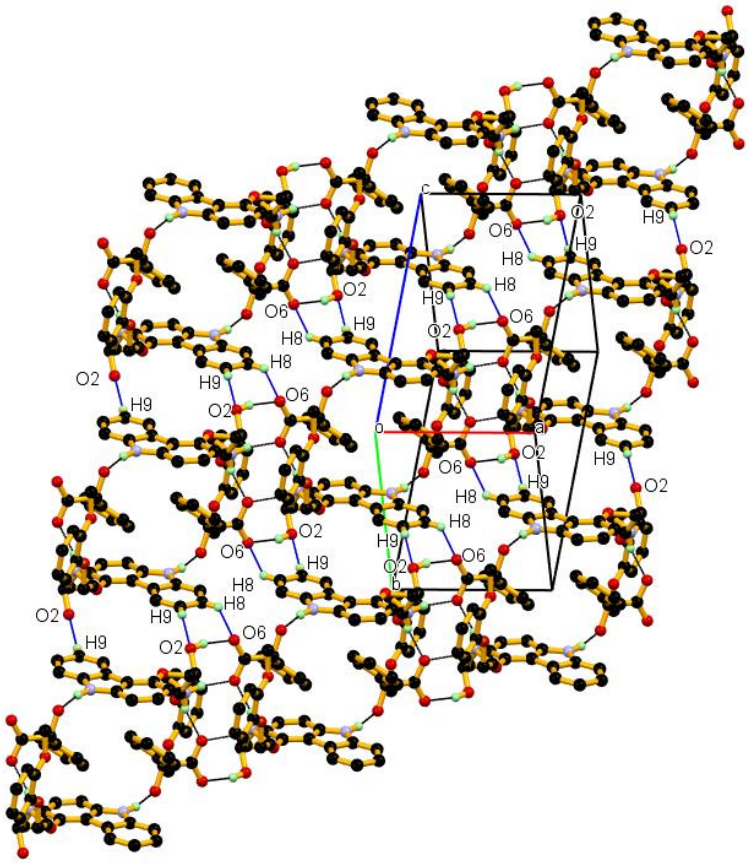

Figure 6. Packing of 1D-dimeric chain, via weak C8–H8···O6 and dimeric C9–H9···O2 hydrogen bonding interaction along the *c*-axis. Blue dotted lines indicate the association of neighboring chains.

Figure 7. Packing of 1D-dimeric chain via weak C–H··· π (C27–H27···Cg4) interaction along *a*-axis.

3.3. PXRD Measurements

PXRD profiles were used for the confirmation of the newly formed crystalline phase in the solid state, as well as to determine the purity of the generated form by comparing it with the simulated pattern from the X-ray single-crystal structure (Figure 8). Every crystalline phase of a compound

displayed its own characteristic PXRD pattern. PXRD profiles of the CVD, DL-MA, and CVD_DL-MA (experimental and simulated) were recorded, and they confirmed the formation of a 1:1 salt of CVD and DL-MA. Furthermore, the overlay of the experimental PXRD pattern of these crystals matched the simulated PXRD pattern obtained from the single-crystal X-ray data, confirming the homogeneity of the sample and ruling out the possibility of the involvement of another phase (Form I). This form is considered as Form I, according to reported results from the previous result [40].

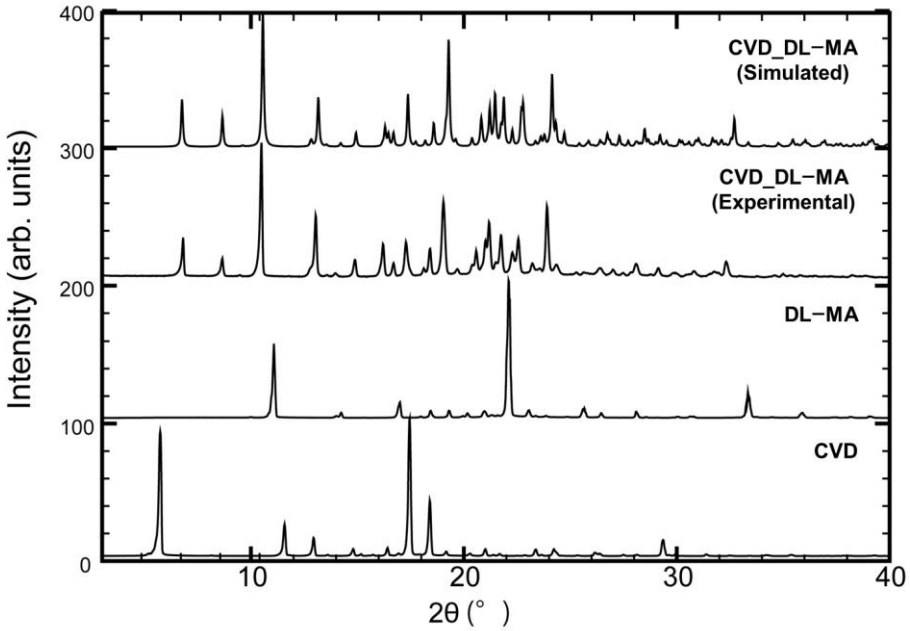

Figure 8. PXRD patterns of CVD_DL-MA (simulated), CVD_DL-MA (experimental), DL-MA, and CVD.

3.4. FT-IR Spectrum

FT-IR is a powerful tool for detecting molecular complexes since the vibrational changes serve as probes for intermolecular interactions in solid materials. A comparison of the FT-IR spectra of the obtained CVD_DL-MA, CVD, and DL-MA (Figure 9) showed numerous changes, confirming that new multi-component crystals were generated. FT-IR analysis was also used to differentiate the salt formation compared to other multi-component crystals (cocrystals), as distinguished by the proton location between the acid and the base [53–55]. In the formation of a salt species, typical carboxylate anions which have a carbonyl stretching band were demonstrated: a strong asymmetrical band below 1600 cm^{-1}, and the appearance of a shoulder between 1505 cm^{-1} and 1610 cm^{-1} where the ionized carboxyl group can be observed [56], not present in the spectra of the individual components. On the other hand, when the frequency of the carbonyl group in carboxylic acid shifted to the higher energy (approximate frequency range of 1700–1730 cm^{-1}), a cocrystal species formed [57]. Examination of the FT-IR spectrum indicated a proton transfer from the salt form to CVD, confirming the salt formation between CVD and DL-MA.

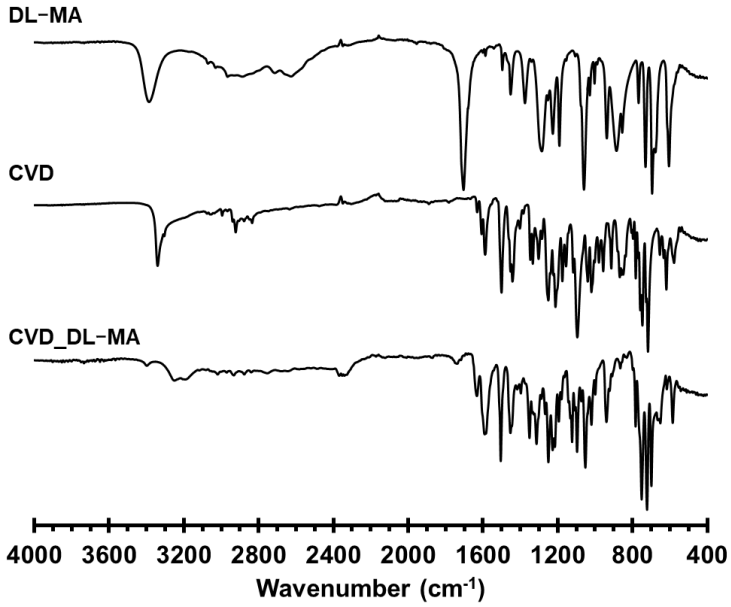

Figure 9. FT-IR spectra of DL-MA, CVD, and CVD_DL-MA.

3.5. Thermal Properties

The thermal properties of the salt were evaluated by DSC and TG measurements. DSC revealed a single sharp endotherm at 169.4 °C, corresponding to melting. This suggested the non-involvement of any phase change before the melting point. TG data revealed that no weight loss before melting confirmed the absence of any solvent or hydrate in the crystal lattice (Figure 10).

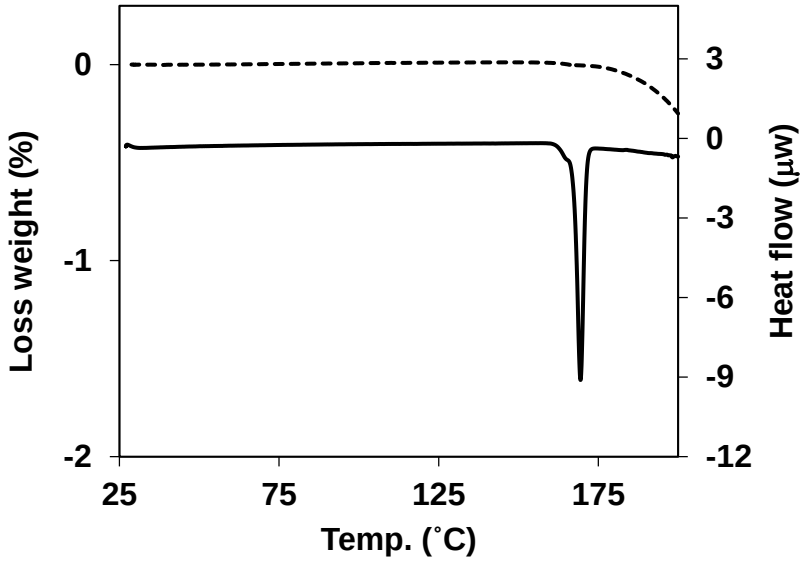

Figure 10. DSC and TG profiles of CVD_DL-MA.

Finally, PXRD, FT-IR, DSC, and TG data of CVD_DL-MA demonstrated good agreement with previously reported data for a Form I [40] stable polymorph. Hence, it was confirmed that the obtained salt was stable Form I.

3.6. Dissolution Studies

The equilibrium solubility of CVD and CVD_DL-MA were 1.2 ± 0.13 and 1.6 ± 0.03 µg/mL, respectively. The equilibrium solubility of the salt was almost 1.3 times as that of CVD alone. Thus,

this work should be emphasized as an example that salt formation can improve the solubility of drugs. Furthermore, this result will be more valuable if it is accompanied by a kinetic aspect, represented by the dissolution rate. As shown in Figure 11, the intrinsic dissolution rate of the CVD_DL-MA was approximately 10.7 times faster than that of CVD alone. Overall, dissolution testing indicated higher CVD in salt samples, emphasizing the importance of the solid state of the investigated formulations, as well as the presence of an excipient that potentially creates a favorable pH environment for the drug upon dissolution as seen for the CVD_DL-MA.

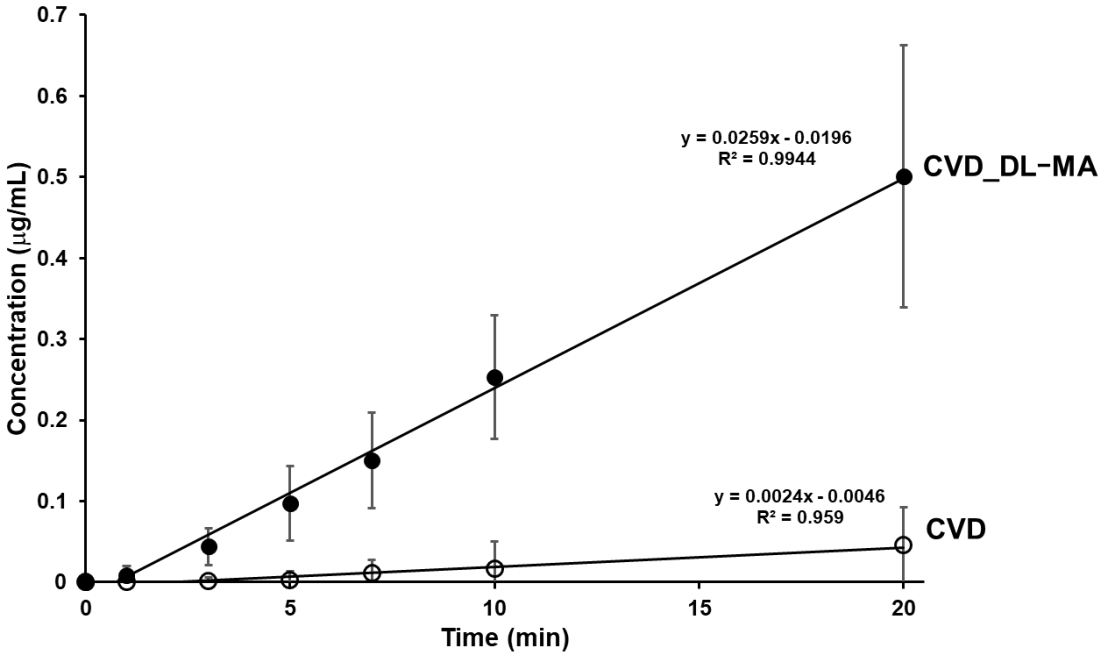

Figure 11. Intrinsic dissolution rate profiles of CVD and CVD_DL-MA.

4. Conclusions

The X-ray structural analysis of the CVD_DL-MA salt revealed the presence of a strong association between the CVD and DL-MA. Protonated CVD formed a dimeric unit bridged with DL-MA anions by strong N^+–H···O^-, O–H···O^- hydrogen bonds. Furthermore, such dimeric units were linked through N–H···O hydrogen bonding to form a 1D-dimeric chain. Neighboring 1D-dimeric chain assembled along the *a*, *b*, and *c*-axis by weak non-covalent interaction. Thermal and powder XRD studies confirmed that the CVD_DL-MA salt was stable Form I. The intrinsic dissolution rate of the CVD_DL-MA was approximately 10.7 times faster than that of CVD alone.

Author Contributions: Conceptualization, N.H. and T.F.; formal analysis, N.H. and D.U.; investigation, N.H., M.I. and D.U.; writing of original draft preparation, N.H., T.F., and M.I.T.; writing of review and editing, T.F., K.F. and E.Y.; visualization, N.H., T.F., M.I.T. and D.U.; supervision, K.F. and E.Y.; project administration, T.F. and E.Y.; N.H. and T.F. contributed equally to this article. All authors have read and agreed to the published version of the manuscript.

Funding: This study was supported by Hoshi University Grant-in-Aid for Leading Research Project grants in 2017 and 2018, and by the OTC Self-Medication Promotion Foundation 2018 (to T.F.).

Acknowledgments: The authors thank Nao Kobayashi for the technical assistance provided in the experimental works.

Conflicts of Interest: The authors declare no conflict of interest.

References

1. Aakeröy, C.B.; Salmon, D.J. Building co-crystals with molecular sense and supramolecular sensibility. *CrystEngComm* **2005**, *7*, 439–448. [CrossRef]
2. Aitipamula, S.; Wong, A.B.H.; Chow, P.S.; Tan, R.B.H. Pharmaceutical salts of haloperidol with some carboxylic acids and artificial sweeteners: Hydrate formation, polymorphism, and physicochemical properties. *Cryst. Growth Des.* **2014**, *14*, 2542–2556. [CrossRef]
3. Morissette, S.L.; Almarsson, O.; Peterson, M.L.; Remenar, J.F.; Read, M.J.; Lemmo, A.V.; Ellis, S.; Cima, M.J.; Gardner, C.R. High-throughput crystallization: Polymorphs, salts, co-crystals and solvates of pharmaceutical solids. *Adv. Drug Deliv. Rev.* **2004**, *56*, 275–300. [CrossRef] [PubMed]
4. Sathisaran, I.; Dalvi, S.V. Engineering cocrystals of poorly water-soluble drugs to enhance dissolution in aqueous medium. *Pharmaceutics* **2018**, *10*. [CrossRef]
5. Schultheiss, N.; Newman, A. Pharmaceutical cocrystals and their physicochemical properties. *Cryst. Growth Des.* **2009**, *9*, 2950–2967. [CrossRef] [PubMed]
6. Sun, C.C. Cocrystallization for successful drug delivery. *Expert Opin. Drug Deliv.* **2013**, *10*, 201–213. [CrossRef]
7. Vishweshwar, P.; McMahon, J.A.; Bis, J.A.; Zaworotko, M.J. Pharmaceutical co-crystals. *J. Pharm. Sci.* **2006**, *95*, 499–516. [CrossRef]
8. Yousef, M.A.E.; Vangala, V.R. Pharmaceutical cocrystals: Molecules, crystals, formulations, medicines. *Cryst. Growth Des.* **2019**, *19*, 7420–7438. [CrossRef]
9. Nauha, E.; Nissinen, M. Co-crystals of an agrochemical active—A pyridine-amine synthon for a thioamide group. *J. Mol. Struct.* **2011**, *1006*, 566–569. [CrossRef]
10. Bučar, D.-K.; Filip, S.; Arhangelskis, M.; Lloyd, G.O.; Jones, W. Advantages of mechanochemical cocrystallisation in the solid-state chemistry of pigments: Colour-tuned fluorescein cocrystals. *CrystEngComm* **2013**, *15*, 6289–6291. [CrossRef]
11. Li, M.; Li, Z.; Zhang, Q.; Peng, B.; Zhu, B.; Wang, J.-R.; Liu, L.; Mei, X. Fine-tuning the colors of natural pigment emodin with superior stability through cocrystal engineering. *Cryst. Growth Des.* **2018**, *18*, 6123–6132. [CrossRef]
12. Bolton, O.; Simke, L.R.; Pagoria, P.F.; Matzger, A.J. High power explosive with good sensitivity: A 2:1 Cocrystal of CL-20:HMX. *Cryst. Growth Des.* **2012**, *12*, 4311–4314. [CrossRef]
13. Millar, D.I.A.; Maynard-Casely, H.E.; Allan, D.R.; Cumming, A.S.; Lennie, A.R.; Mackay, A.J.; Oswald, I.D.H.; Tang, C.C.; Pulham, C.R. Crystal engineering of energetic materials: Co-crystals of CL-20. *CrystEngComm* **2012**, *14*, 3742–3749. [CrossRef]
14. Bolton, O.; Matzger, A.J. Improved stability and smart-material functionality realized in an energetic cocrystal. *Angew. Chem. Int. Ed.* **2011**, *50*, 8960–8963. [CrossRef]
15. Thayer, A.M. Form and function. *Chem. Eng. News* **2007**, *85*, 17–30. [CrossRef]
16. Prohotsky, D.L.; Zhao, F. A survey of top 200 drugs-inconsistent practice of drug strength expression for drugs containing salt forms. *J. Pharm. Sci.* **2012**, *101*, 1–6. [CrossRef]
17. Kalepu, S.; Nekkanti, V. Insoluble drug delivery strategies: Review of recent advances and business prospects. *Acta Pharm. Sin. B* **2015**, *5*, 442–453. [CrossRef]
18. Liversidge, G.G.; Cundy, K.C. Particle size reduction for improvement of oral bioavailability of hydrophobic drugs: I. Absolute oral bioavailability of nanocrystalline danazol in beagle dogs. *Int. J. Pharm.* **1995**, *125*, 91–97. [CrossRef]
19. Müller, R.H.; Peters, K. Nanosuspensions for the formulation of poorly soluble drugs: I. Preparation by a size-reduction technique. *Int. J. Pharm.* **1998**, *160*, 229–237. [CrossRef]
20. Shaikh, J.; Ankola, D.D.; Beniwal, V.; Singh, D.; Kumar, M.N. Nanoparticle encapsulation improves oral bioavailability of curcumin by at least 9-fold when compared to curcumin administered with piperine as absorption enhancer. *Eur. J. Pharm. Sci.* **2009**, *37*, 223–230. [CrossRef]
21. Ohara, T.; Kitamura, S.; Kitagawa, T.; Terada, K. Dissolution mechanism of poorly water-soluble drug from extended release solid dispersion system with ethylcellulose and hydroxypropylmethylcellulose. *Int. J. Pharm.* **2005**, *302*, 95–102. [CrossRef]

22. Hasegawa, S.; Hamaura, T.; Furuyama, N.; Kusai, A.; Yonemochi, E.; Terada, K. Effects of water content in physical mixture and heating temperature on crystallinity of troglitazone-PVP K30 solid dispersions prepared by closed melting method. *Int. J. Pharm.* **2005**, *302*, 103–112. [CrossRef] [PubMed]
23. Jambhekar, S.S.; Breen, P. Cyclodextrins in pharmaceutical formulations II: Solubilization, binding constant, and complexation efficiency. *Drug Discov. Today* **2016**, *21*, 363–368. [CrossRef] [PubMed]
24. Rajput, L.; Sanphui, P.; Desiraju, G.R. New Solid Forms of the Anti-HIV Drug Etravirine: Salts, Cocrystals, and Solubility. *Cryst. Growth Des.* **2013**, *13*, 3681–3690. [CrossRef]
25. Banerjee, R.; Bhatt, P.M.; Ravindra, N.V.; Desiraju, G.R. Saccharin salts of active pharmaceutical ingredients, their crystal structures, and increased water solubilities. *Cryst. Growth Des.* **2005**, *5*, 2299–2309. [CrossRef]
26. Karimi-Jafari, M.; Padrela, L.; Walker, G.M.; Croker, D.M. Creating cocrystals: A review of pharmaceutical cocrystal preparation routes and applications. *Cryst. Growth Des.* **2018**, *18*, 6370–6387. [CrossRef]
27. Cao, H.-L.; Zhou, J.-R.; Cai, F.-Y.; Lü, J.; Cao, R. Two-component pharmaceutical cocrystals regulated by supramolecular synthons comprising primary N···H···O interactions. *Cryst. Growth Des.* **2019**, *19*, 3–16. [CrossRef]
28. Thorat, S.H.; Patwadkar, M.V.; Gonnade, R.G.; Vaidhyanathan, R. Capturing a novel metastable polymorph of the anticancer drug gefitinib. *CrystEngComm* **2014**, *16*, 8638–8641. [CrossRef]
29. Zhu, B.; Fang, X.; Zhang, Q.; Mei, X.; Ren, G. Study of crystal structures, properties, and form transformations among a polymorph, hydrates, and solvates of apatinib. *Cryst. Growth Des.* **2019**, *19*, 3060–3069. [CrossRef]
30. Colucci, W.S.; Packer, M.; Bristow, M.R.; Gilbert, E.M.; Cohn, J.N.; Fowler, M.B.; Krueger, S.K.; Hershberger, R.; Uretsky, B.F.; Bowers, J.A.; et al. Carvedilol inhibits clinical progression in patients with mild symptoms of heart failure. *Circulation* **1996**, *94*, 2800–2806. [CrossRef]
31. Packer, M.; Bristow, M.R.; Cohn, J.N.; Colucci, W.S.; Fowler, M.B.; Gilbert, E.M.; Shusterman, N.H. The effect of carvedilol on morbidity and mortality in patients with chronic heart failure. *N. Engl. J. Med.* **1996**, *334*, 1349–1355. [CrossRef]
32. Dargie, H.J. Effect of carvedilol on outcome after myocardial infarction in patients with left-ventricular dysfunction: The CAPRICORN randomised trial. *Lancet* **2001**, *357*, 1385–1390. [CrossRef]
33. Amidon, G.L.; Lennernas, H.; Shah, V.P.; Crison, J.R. A theoretical basis for a biopharmaceutic drug classification: The correlation of in vitro drug product dissolution and in vivo bioavailability. *Pharm. Res.* **1995**, *12*, 413–420. [CrossRef]
34. Wei, L.; Sun, P.; Nie, S.; Pan, W. Preparation and evaluation of SEDDS and SMEDDS containing carvedilol. *Drug Dev. Ind. Pharm.* **2005**, *31*, 785–794. [CrossRef]
35. Mahmoud, E.A.; Bendas, E.R.; Mohamed, M.I. Preparation and evaluation of self-nanoemulsifying tablets of carvedilol. *AAPS PharmSciTech* **2009**, *10*, 183–192. [CrossRef]
36. Liu, D.; Xu, H.; Tian, B.; Yuan, K.; Pan, H.; Ma, S.; Yang, X.; Pan, W. Fabrication of carvedilol nanosuspensions through the anti-solvent precipitation-ultrasonication method for the improvement of dissolution rate and oral bioavailability. *AAPS PharmSciTech* **2012**, *13*, 295–304. [CrossRef]
37. Zhang, Y.; Zhi, Z.; Li, X.; Gao, J.; Song, Y. Carboxylated mesoporous carbon microparticles as new approach to improve the oral bioavailability of poorly water-soluble carvedilol. *Int. J. Pharm.* **2013**, *454*, 403–411. [CrossRef]
38. Hirlekar, R.; Kadam, V. Preparation and characterization of inclusion complexes of carvedilol with methyl-β-cyclodextrin. *J. Incl. Phenom. Macrocycl. Chem.* **2009**, *63*, 219–224. [CrossRef]
39. Diniz, L.F.; Carvalho, P.S.; da Nova Mussel, W.; Yoshida, M.I.; Diniz, R.; Fernandes, C. Racemic salts and solid solutions of enantiomers of the antihypertensive drug carvedilol. *Cryst. Growth Des.* **2019**, *19*, 4498–4509. [CrossRef]
40. Hiendrawan, S.; Widjojokusumo, E.; Veriansyah, B.; Tjandrawinata, R.R. Pharmaceutical salts of carvedilol: Polymorphism and physicochemical properties. *AAPS PharmSciTech* **2017**, *18*, 1417–1425. [CrossRef]
41. Prado, L.D.; Rocha, H.V.A.; Resende, J.A.L.C.; Ferreira, G.B.; de Figuereido Teixeira, A.M.R. An insight into carvedilol solid forms: Effect of supramolecular interactions on the dissolution profiles. *CrystEngComm* **2014**, *16*, 3168–3179. [CrossRef]
42. Bolla, G.; Nangia, A. Clofazimine Mesylate: A High Solubility Stable Salt. *Cryst. Growth Des.* **2012**, *12*, 6250–6259. [CrossRef]
43. Gunnam, A.; Nangia, A.K. High-Solubility Salts of the Multiple Sclerosis Drug Teriflunomide. *Cryst. Growth Des.* **2019**, *19*, 5407–5417. [CrossRef]

44. Putra, O.D.; Umeda, D.; Nugraha, Y.P.; Furuishi, T.; Nagase, H.; Fukuzawa, K.; Uekusa, H.; Yonemochi, E. Solubility improvement of epalrestat by layered structure formation via cocrystallization. *CrystEngComm* **2017**, *19*, 2614–2622. [CrossRef]
45. Putra, O.D.; Umeda, D.; Nugraha, Y.P.; Nango, K.; Yonemochi, E.; Uekusa, H. Simultaneous improvement of epalrestat photostability and solubility via cocrystallization: A case study. *Cryst. Growth Des.* **2018**, *18*, 373–379. [CrossRef]
46. Dwichandra Putra, O.; Umeda, D.; Fujita, E.; Haraguchi, T.; Uchida, T.; Yonemochi, E.; Uekusa, H. solubility improvement of benexate through salt formation using artificial sweetener. *Pharmaceutics* **2018**, *10*, 64. [CrossRef]
47. Ainurofiq, A.; Mauludin, R.; Mudhakir, D.; Umeda, D.; Soewandhi, S.N.; Putra, O.D.; Yonemochi, E. Improving mechanical properties of desloratadine via multicomponent crystal formation. *Eur. J. Pharm. Sci.* **2018**, *111*, 65–72. [CrossRef]
48. Teraoka, R.; Fukami, T.; Furuishi, T.; Nagase, H.; Ueda, H.; Tode, C.; Yutani, R.; Kitagawa, S.; Sakane, T. Improving the solid-state photostability of furosemide by its cocrystal formation. *Chem. Pharm. Bull.* **2019**, *67*, 940–944. [CrossRef]
49. Higashi, T. *Calculated Using ABSCOR: Empirical Absorption Correction Based on Fourier Series Approximation*; Rigaku: The Woodland, TX, USA, 1994.
50. Burla, M.C.; Caliandro, R.; Camalli, M.; Carrozzini, B.; Cascarano, G.L.; De Caro, L.; Giacovazzo, C.; Polidori, G.; Spagna, R. SIR2004: An improved tool for crystal structure determination and refinement. *J. Appl. Crystallogr.* **2005**, *38*, 381–388. [CrossRef]
51. Sheldrick, G. A short history of SHELX. *Acta Crystallogr. Sect. A* **2008**, *64*, 112–122. [CrossRef] [PubMed]
52. Macrae, C.F.; Bruno, I.J.; Chisholm, J.A.; Edgington, P.R.; McCabe, P.; Pidcock, E.; Rodriguez-Monge, L.; Taylor, R.; van de Streek, J.; Wood, P.A. Mercury CSD 2.0—New features for the visualization and investigation of crystal structures. *J. Appl. Crystallogr.* **2008**, *41*, 466–470. [CrossRef]
53. Parmar, V.K.; Shah, S.A. Hydrochloride salt co-crystals: Preparation, characterization and physicochemical studies. *Pharm. Dev. Technol.* **2013**, *18*, 443–453. [CrossRef]
54. Arenas-García, J.I.; Herrera-Ruiz, D.; Mondragón-Vásquez, K.; Morales-Rojas, H.; Höpfl, H. Co-crystals of active pharmaceutical ingredients—Acetazolamide. *Cryst. Growth Des.* **2010**, *10*, 3732–3742. [CrossRef]
55. Stevanus, H.; Bambang, V.; Edward, W.; Sundani Nurono, S.; Saleh, W.; Raymond, R.T. Simultaneous cocrystallization and micronization of paracetamol-dipicolinic acid cocrystal by supercritical antisolvent (SAS). *Int. J. Pharm. Pharm. Sci.* **2016**, *8*, 89–98.
56. Mishra, J.; Lobmann, K.; Grohganz, H.; Rades, T. Influence of preparation technique on co-amorphization of carvedilol with acidic amino acids. *Int. J. Pharm.* **2018**, *552*, 407–413. [CrossRef]
57. Swapna, B.; Maddileti, D.; Nangia, A. Cocrystals of the tuberculosis drug isoniazid: Polymorphism, isostructurality, and stability. *Cryst. Growth Des.* **2014**, *14*, 5991–6005. [CrossRef]